ACS APPLIED NANO MATERIALS

www.acsanm.org Article

Ordered-Range Tuning of Flash Graphene for Fast-Charging Lithium-Ion Batteries

Hongyan Yang, Lanju Sun, Shengliang Zhai, Xiao Wang, Chengcheng Liu, Hao Wu,* and Weiqiao Deng*

Cite This: https://doi.org/10.1021/acsanm.2c04717 Read Online

ACCESS | Metrics & More | Article Recommendations | Supporting Information

ABSTRACT: Graphene has yet to be mass produced, so practical fast-charging lithium-ion battery (LIB) prototypes based on graphene are scarce. Graphene suffers from long in-plane and reluctant in-depth lithium diffusion due to its defect-free atomic arrangement, resulting in unsatisfactory rate performance as LIB anodes. In this work, combinatorial flash joule heating and ball milling treatment are implemented to enable gram-scale production of graphene in seconds (known as flash graphene, FG) and in-plane ordered-range modulation of graphene architectures. Following the ball milling, the defect-deficient turbostratic FG is transformed to defect-rich cracked FG (CFG), which has shortened ordered ranges and larger interlayer spacings. The CFG anode outperforms FG, commercial carbon black, and graphite electrodes in terms of specific capacity and rate performance due to open channels and shortened pathways for Li^+ transport. Moreover, it shows outstanding cycling stability with a high capacity retention of 99% at the 500th cycle. Furthermore, it works well with the $LiFePO_4$ cathode, enabling fast-charging LIB full battery with a state of charge of 77 and 62% at 2C and 4C, respectively. This research on graphene production and structural engineering provides a practical application for the commercial potential of fast-charging LIBs.

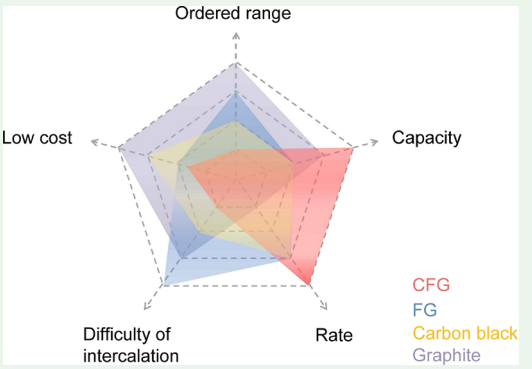

KEYWORDS: *flash graphene, fast-charging, lithium-ion batteries, anodes, ball milling*

INTRODUCTION

Due to the advantages of high energy density, long cycle life, and no memory effect, lithium-ion batteries (LIBs) have been widely used in portable electronic devices, electric vehicles, and smart grids.[1−3] With the increasing demand for short charging time in the consumer electronics and power battery markets, fast-charging technology has become a long-term strategic goal in the development of LIBs in recent years.[4,5] Extensive research demonstrate that fast-charging anode materials are one of the keys to realizing fast-charging LIBs because the well-known anode materials (e.g., graphite) have shown slow lithium diffusion rates, resulting in poor rate performance.[6−8] Commercial graphite is widely applied in LIBs anodes because of its abundance, low cost, and high ionic and electric conductivity.[8] Moreover, it exhibits excellent initial Coulomb efficiency (ICE) and cycling stability. Yet, Li^+ is obliged to diffuse through long ordered ranges of graphite planes instead of migrating across the multilayers, which results in a low Li^+ diffusion rate. Other than the long in-plane Li^+ diffusion distance, lithium deposition and short circuit tend to happen owing to the narrow interlayer spacing of graphite (~3.35 Å), which also limits its fast-charging capability.[1,9]

As an alternative, graphene shows high Li^+ diffusivity (10^{-7} to 10^{-6} cm^2 s^{-1}) and a higher theoretical capacity of 744 mAh g^{-1} than that of graphite (372 mAh g^{-1}), which thus has been highlighted as a promising anode material that may fulfill fast-charging LIBs.[10,11] However, routine synthesis of graphene by chemical vapor deposition and tedious reduction of graphene oxide is costly and suffers from low production yield, making them suboptimal manipulations.[12,13] Very recently, Tour and co-workers proposed a flash joule heating (FJH) strategy to fabricate gram-scale graphene, named flash graphene (FG), using commercial carbon black (and even plastic wastes) within seconds, making it an economic and high-throughput method.[14] Unfortunately, the resultant turbostratic arranged graphene layers in the FG exhibit low capacities as LIB anodes, which fail to meet the requirements for fast-charging.[4] The in-depth migration of Li^+ remains resistant due to the defect-free atomic arrangement of graphene shells. Therefore, shortening the in-plane ordered ranges of the FG through facile fracturing could open the Li^+ transport channels and shorten Li^+ diffusion pathways.[15] Meanwhile, the interlayer spacing would better be enlarged following such implementations, by which the Li^+

Received: October 28, 2022
Accepted: January 30, 2023

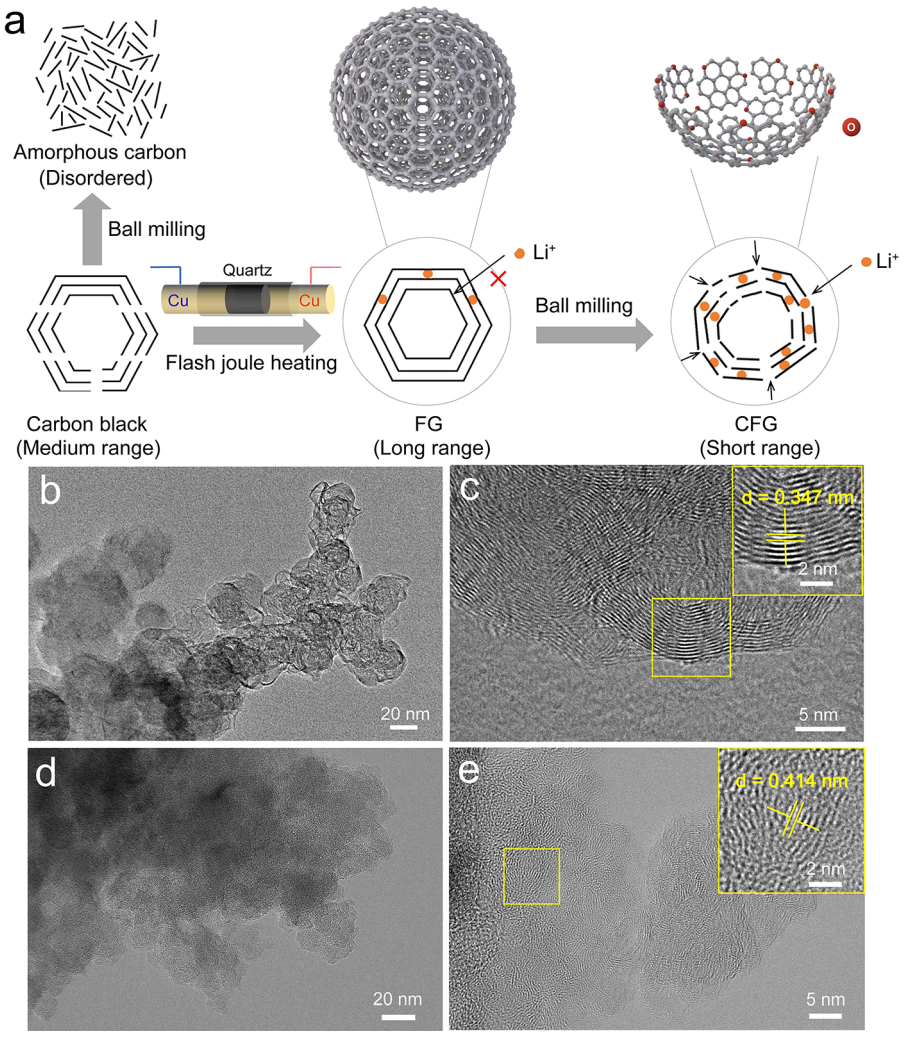

Figure 1. (a) Schematic illustration of the morphological structure of the conversion from CB to CFG. (b) TEM image and (c) HRTEM image of FG. (d) TEM image and (e) HRTEM image of CFG.

diffusion kinetics could be improved, leading to faster Li^+ insertion/extraction and eventually realizing fast-charging.[16]

Bearing these in mind, a combinatorial FJH and ball milling (BM) strategy is adopted to synthesize short-range ordered cracked flash graphene (CFG), which qualifies as fast-charging LIB anodes. Commercial carbon black (CB) is served as the starting carbon precursors, which undergoes FJH to form FG, and, subsequently, BM treatment to obtain the CFG. The as-synthesized CFG shows ordered structures in a shorter range compared to that of FG, which could shorten the paths for Li^+ diffusion and electron transfer. Moreover, the CFG with more defects and O dopants exhibits increased surface areas and enlarged interlayer spacings, which lead to more reactive sites and accelerated Li^+ diffusion kinetics.[17] As a result, the CFG anode delivers significantly improved specific capacities than that of FG. Meanwhile, it is superior to commercial carbon black and graphite electrodes. Moreover, the CFG anode shows outstanding cycling stability with capacity retention of 99% (500th) and 90% (600th) at 1 and 5 A g^{-1}, respectively. Furthermore, the full cells assembled by CFG anode and $LiFePO_4$ (LFP) cathode exhibit a state of charge (SOC) of 77 and 62% at 2C and 4C respectively, which enable fast-charging LIBs. The proposed combinatorial FJH and BM strategy provides a low-cost and high-throughput way to produce anode materials for fast-charging LIBs.

RESULTS AND DISCUSSION

The regulation of the ordered structure range and corresponding synthetic procedures are schematically illustrated in Figure 1a. Briefly, CB is used as the starting carbon source to prepare FG through FJH operation. Subsequently, BM treatment under argon atmosphere is adopted to make fractures in the FG, rendering the formation of CFG. The FJH is generated during the fast discharging process using a homemade setup (Figure S1). The microstructure evolution of the as-prepared samples was revealed using scanning electron microscopy (SEM) and transmission electron microscopy (TEM). Both CB and FG show discrete nanoparticles, as indicated by the SEM images in Figure S2. A typical TEM image of CB reveals that the nanoparticle size ranges mainly from 20 to 60 nanometers (Figure S3). A high-resolution TEM (HRTEM) image indicates turbostratic lattice fringes with a *d*-spacing of 0.342 nm (Figure S4), in which several fractures and atomic defects are obtained, making ordered ranges of about 2−5 nm. After FJH, the resultant FG retains nanosized grains (Figure 1b, TEM). The HRTEM image reveals continuous turbostratic lattice fringes with scarce fractures and defects (Figure 1c and

https://doi.org/10.1021/acsanm.2c04717
ACS Appl. Nano Mater. XXXX, XXX, XXX−XXX

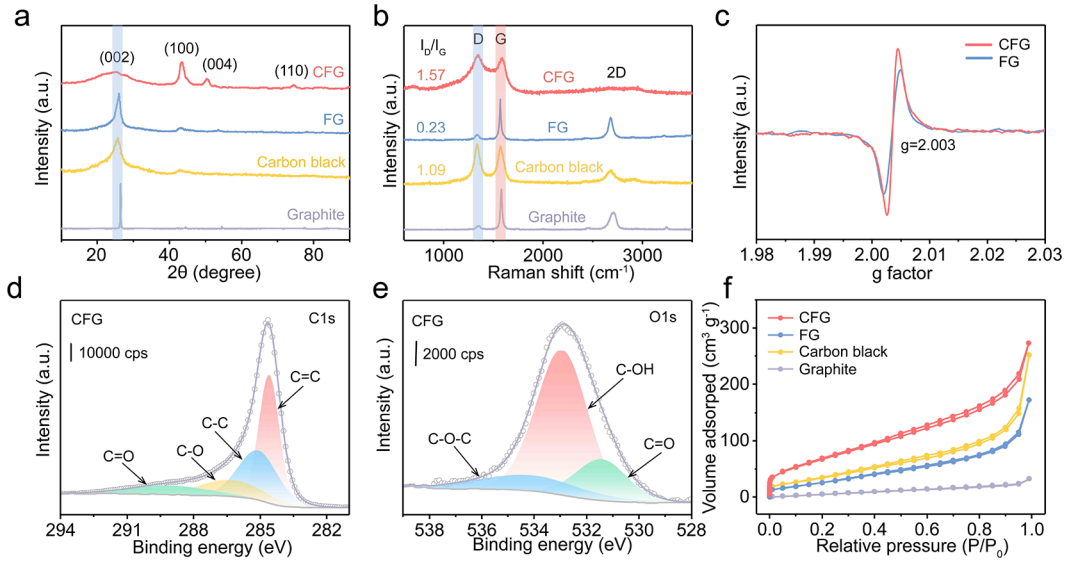

Figure 2. Physical−chemical properties of the as-obtained samples. (a) XRD patterns; (b) Raman spectra; (c) ESR spectra; (d) high-resolution XPS analysis of C 1s and (e) O 1s for CFG; (f) nitrogen adsorption/desorption isotherms.

Figure S5). This longer ordered range in the lattice can be ascribed to defect healing in the FJH process, which has almost no impact on the *d*-spacing (0.347 nm).

BM, an inexpensive technique, is commonly used to downsize materials by shear and compression force.[18] Therefore, BM could be adopted to shorten the ordered range of the FG lattice. TEM and SEM images show that the BM treatment induces obvious particle aggregation, where the particulate size has been increased to hundreds of nanometers (Figure 1d and Figure S6). Encouragingly, the turbostratic lattice fringe character disappears, while enormous fractures and defects appear in the BM-treated FG, revealed further by the HRTEM image (Figure 1e and Figure S7). The *d*-spacing has been enlarged accordingly, ranging from 0.367 to 0.414 nm, and the corresponding ordered range has been shortened to below 2 nm. Therefore, the BM post-treatment has successfully broken long-range ordered FG into short-range ordered cracked fragments (denoted as CFG). In contrast, the medium-range ordered CB after direct BM manipulation results in slight aggregation (Figure S8), which shows a quasi-amorphous character as indicated by the HRTEM image in Figure S9. Therefore, it is concluded that the ordered range of the starting CB specie can be tuned by the FJH and BM implementation, leading to the formation of FG, CFG, and amorphous carbon.

X-ray diffraction (XRD) was further performed to reveal the crystallinity of the CB, FG, CFG, and graphite. As displayed in Figure 2a, both CB and FG show (002) diffraction peaks at 2θ = 25.72°, which are a little lower than that of graphite (26.28°). The corresponding layer-to-layer *d*-spacing is calculated to be 0.346 nm,[18] which is slightly larger than the latter one (0.339 nm), agreeing with the results observed in HRTEM images (Figure S10). As for the CFG, the (002) peak is broader and weaker in intensity than that of the FG, implying that CFG has bigger sizes, lower crystallinity, and increased disorder.[17−19] These characters are in line with the TEM results.

Raman spectroscopy is widely used to characterize the quality and defects in graphene because many details can be extracted from the fine structure of graphene.[19,20] As shown in Figure 2b, the CB shows an obvious D band at 1336 cm^{-1}, which is attributed to the disorder and defects in the crystal structure. After FJH, FG shows a negligible D band with a low ratio of the D-to-G-band intensity (I_D/I_G = 0.23) due to the rearrangement of the disordered carbon into ordered layered FG via the FJH. The FG has displayed typical TS_1 (at 1881 cm^{-1}) and TS_2 (at 2049 cm^{-1}) peaks, confirming that the CB has been converted into turbostratic graphene successfully (Figure S11).[14] Moreover, the I_D/I_G ratio is comparable to that of graphite, demonstrating highly symmetrical sp^2 hybridization carbon with tiny defects in the crystal structures.[19] In contrast, the CFG shows a broader and stronger D band with a much larger I_D/I_G value of 1.57, which indicates that BM introduces massive defects to the parental FG. Furthermore, electron spin resonance (ESR) is conducted to verify the introduction of defects. The CFG exhibits a stronger ESR signal at g = 2.003, corresponding to unpaired electrons of defective sites,[17,21] than that of the FG as observed in Figure 2c, which implies more defects formed at edges and interfaces in the CFG. The induction of oxygen dopants into the FG could be ascribed to high-energy mechanical vibration during BM, which may serve as extra binding sites for Li ions.

X-ray photoelectron spectroscopy (XPS) measurements were performed to investigate the chemical composition of the four samples. XPS surveys identify the presence of C and O elements for each sample (Figure S12), in which the CFG shows the highest O/C atomic ratio, indicating the most O dopants. Four deconvoluted peaks located at 284.6, 285.1, 286.3, and 289.1 eV in the high-resolution C 1s peak of the CFG can be assigned to C═C, C−C, C−O, and C═O components, respectively (Figure 2d).[20] The sp^3 hybridization component and O-containing species have been dramatically increased following the BM treatment (Figure 2e and Figure S13), which agrees with the Raman and ESR results. Moreover, Fourier transform infrared (FTIR) spectrometry shown in Figure S14 shows that the characteristic bond of C═O at 1709 cm^{-1} appeared and the intensity of C−O−C at 1340 cm^{-1} is greatly increased in the CFG, which also verify the increase of the O-containing species.

https://doi.org/10.1021/acsanm.2c04717
ACS Appl. Nano Mater. XXXX, XXX, XXX−XXX

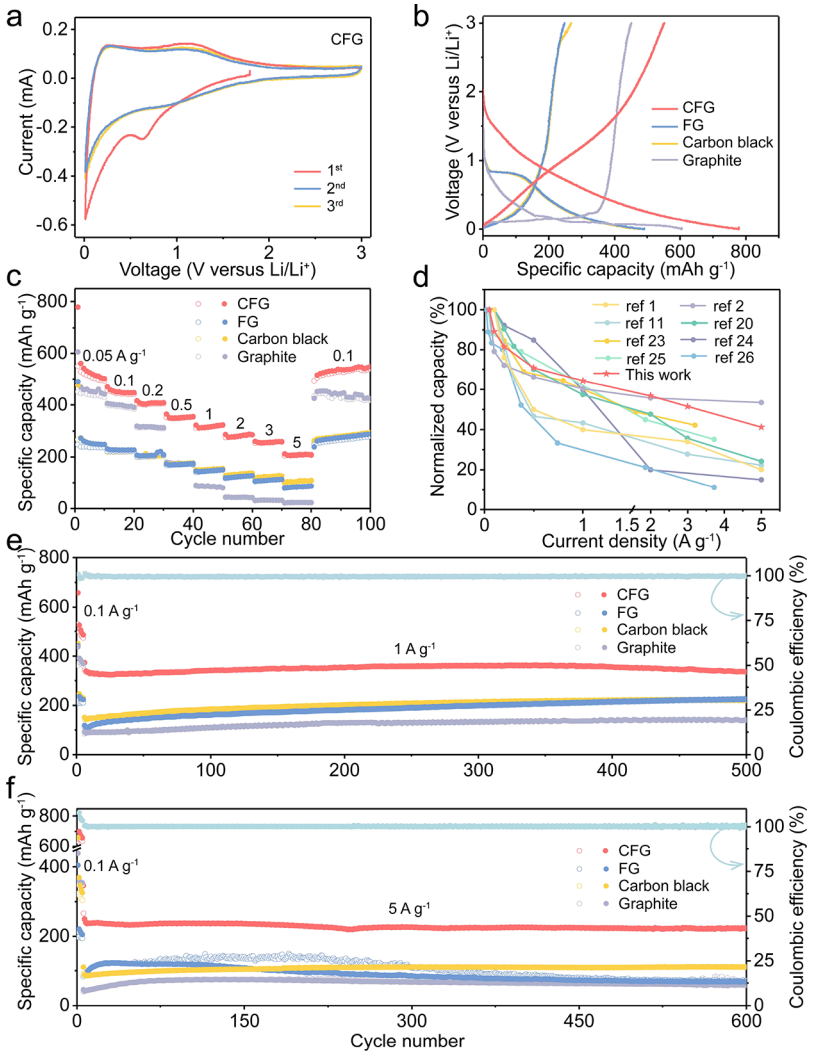

Figure 3. Electrochemical characteristics of the various anodes in half cells. (a) First three CV curves; (b) first discharge/charge curves at 0.05 A g^{-1}; (c) rate capabilities at different current densities from 0.05 to 5 A g^{-1}; (d) comparison of capacities between this work and other literature; (e) cycling stability of the four electrodes at 1 A g^{-1} and (f) 5 A g^{-1}.

N_2 adsorption−desorption isotherms were carried out to characterize the surface area and pore size distribution. As shown in Figure 2f, the CFG exhibits a typical type IV isotherm, which suggests micro- and mesoporous features.[22] It shows a specific surface area as high as 155.6 m^2 g^{-1}, which is higher than that of the FG (114.2 m^2 g^{-1}). The increased surface areas mainly stem from nanopores produced by BM. Moreover, it exhibits a large total pore volume of 0.423 cm^{-3} g^{-1} (Table S1), which is conducive to contact with the electrolyte and active sites. The pore size of FG based on the adsorption branch was around 2.6 nm (Figure S15), which increased to 4.2 nm after BM, indicating that the BM process could enlarge the pore size.[22] Compared with graphene layers, Li^+ storing in pores is conducive to minimizing volume expansion during the discharge/charge process, which could enhance cycling stability.

The electrochemical behavior of the sample as LIB anodes was performed in the voltage range of 0.01 to 3 V (vs Li^+/Li). Figure 3a shows the cyclic voltammetry (CV) curves of the CFG anode at a scan rate of 0.1 mV s^{-1}. A typical cathodic peak located at 0.63 V emerges in the first cycle, which then disappears in the following cycles. This corresponds to the formation of solid electrolyte interphase (SEI) layers on the electrode surface, which results in a capacity loss during the first cycling process.[20] Moreover, another anodic peak at 1.2 V refers to Li^+ extraction from the defects in the CFG, such as the pores, edges, and corners of the short ordered-range layers.[1,20] Previously report indicates that the weak peaks at higher potential could be ascribed to the heteroatoms on the surface of CFG.[1,22] Encouragingly, the CV profiles almost overlap after the first cycle, manifesting good reversibility and structural stability of the CFG anode. Figure 3b shows initial discharge−charge profiles of the CFG, FG, CB, and graphite anodes at a current density of 0.05 A g^{-1}. The CFG electrode exhibits an initial discharge and charge capacity of 778 and 551 mAh g^{-1} respectively, corresponding to an initial Coulombic efficiency (ICE) of 71%. This value is much higher than those of CB (51%) and FG (56%) and comparable to that of commercial graphite (75%). The high ICE of the CFG implies its great potential in practical application as anode materials.

The rate performance of the four electrodes was further evaluated as shown in Figure 3c. The CB and FG electrodes show almost overlapped capacities at current densities ranging from 0.05 to 2 A g^{-1}, while the former electrode exhibits

https://doi.org/10.1021/acsanm.2c04717
ACS Appl. Nano Mater. XXXX, XXX, XXX−XXX

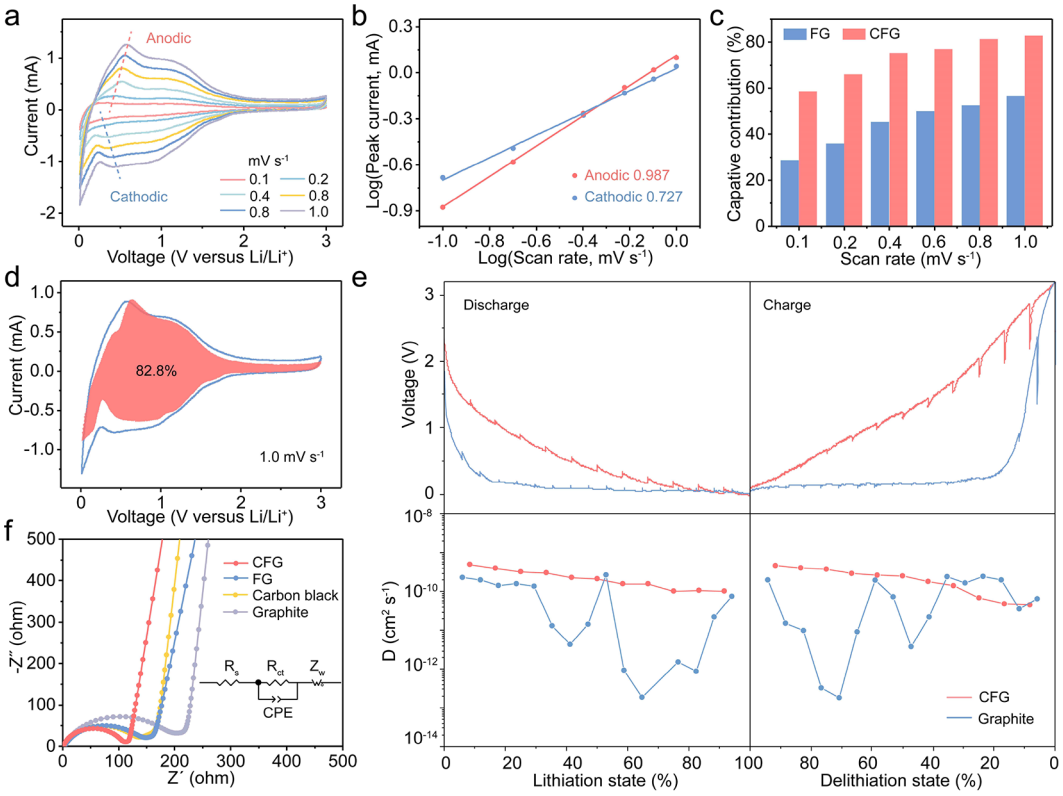

Figure 4. Electrochemical kinetic performance of various electrodes. (a) CV curves of CFG at different scan rates from 0.1 to 1.0 mV s^{-1}; (b) plot of log(i) versus log(v) of anodic/cathodic peaks from CV; (c) the capacitive contribution of FG and CFG at various scan rates; (d) capacitive-controlling contributions (red) of CFG at 1.0 mV s^{-1}; (e) GITT patterns and the calculated diffusion coefficient of Li^+ during the charge/discharge process; (f) Nyquist plots of the as-obtained materials before cycling.

slightly higher capacities than the latter at higher current densities of 3 and 5 A g^{-1}. This could be ascribed to a slower Li^+ diffusion kinetic of the FG than that of the CB, where the former has longer ordered-range structures. Notably, although graphite shows higher capacities under low current densities (0.05 to 0.2 A g^{-1}) than that of CB and FG, the capacities at higher current densities (>1 A g^{-1}) are inferior to the other two electrodes. The poor rate performance of graphite might be originated from its long ordered-range structure, in which the kinetic of Li^+ diffusion is slow.[1] Although the CB and FG electrodes exhibit excellent rate performance, their capacities are limited to 250 mAh g^{-1}. In contrast, the CFG electrode exhibits reversible specific capacities of 501, 447, 409, 355, 323, and 285 mAh g^{-1} at the current densities of 0.05, 0.1, 0.2, 0.5, 1, and 2 A g^{-1}, respectively. The capacities at each current density are almost two times as high as the FG and CB electrodes. More strikingly, the CFG could deliver capacities of 258 and 210 mAh g^{-1} at higher current densities of 3 and 5 A g^{-1}, respectively, which are nearly 10-fold higher than that of the graphite electrode (23 mAh g^{-1}). Moreover, the reversible capacity recovers to 500 mAh g^{-1} as the current density returns to 0.05 A g^{-1}, which indicates the outstanding reversibility of the CFG electrode. As summarized in Figure 3d, such a high rate performance of the CFG electrode surpasses most previously reported graphene-based anodes.[1,2,11,20,23−26] The fast ion and electron transport in the short-range ordered CFG might be responsible for outstanding rate performance.

Furthermore, long-term durability, a key parameter to evaluate the practical applicability,[20,27] is tested for all four electrodes. As shown in Figure 3e and Figure S16, all these electrodes show excellent capacity retention and nearly 100% CEs at the current density of 1 A g^{-1}. Specifically, the CFG exhibits a capacity of 340 mAh g^{-1} with a capacity retention of 99% over 500 cycles. At 5 A g^{-1}, it shows a capacity of 249 mAh g^{-1} (Figure 3f), which is superior to that of the FG, CB, and graphite (90.3, 88.8, and 43 mAh g^{-1}, respectively). The capacity retention reaches 90% over 600 cycles for the CFG electrode. The corresponding CE shown in Figure S17 is nearly 100%, while the CEs of the FG and graphite electrodes decrease gradually after 50 and 200 cycles, respectively. In contrast, the CE of the CFG electrode is nearly 100% at 5 A g^{-1}, further confirming the stable inherent microstructure of the CFG during the electrochemical reactions. The excellent electrochemical performances imply that the CFG as anodes may enable fast-charging LIBs.

To gain deep insight into the excellent rate capability of the CFG and FG, the Li^+ storage kinetic was first investigated by CV analysis (Figure 4a and Figure S18). Figure 4a depicts that both anodic and cathodic peaks in the non-ideal, triangular shape of CV curves of the CFG electrode slightly shift with the increase of scan rate from 0.1 to 1.0 mV s^{-1}, indicating good electrical conductivity and fast ion transportation. To explain the Li^+ storage mechanism, the peak currents (i) and scan rates (v) are extracted and used to calculate the b value following the power-law relationship $i = av^b$, where the b value is an indicator of the charge storage kinetics.[27] When the b value equals to 0.5, the electrochemical behavior is a diffusion-controlled process, whereas when it is close to 1, it indicates a capacitive-dominant process.[27] As shown in Figure 4b, the anodic and cathodic b values are calculated to be 0.987 and 0.727, respectively, which

https://doi.org/10.1021/acsanm.2c04717
ACS Appl. Nano Mater. XXXX, XXX, XXX−XXX

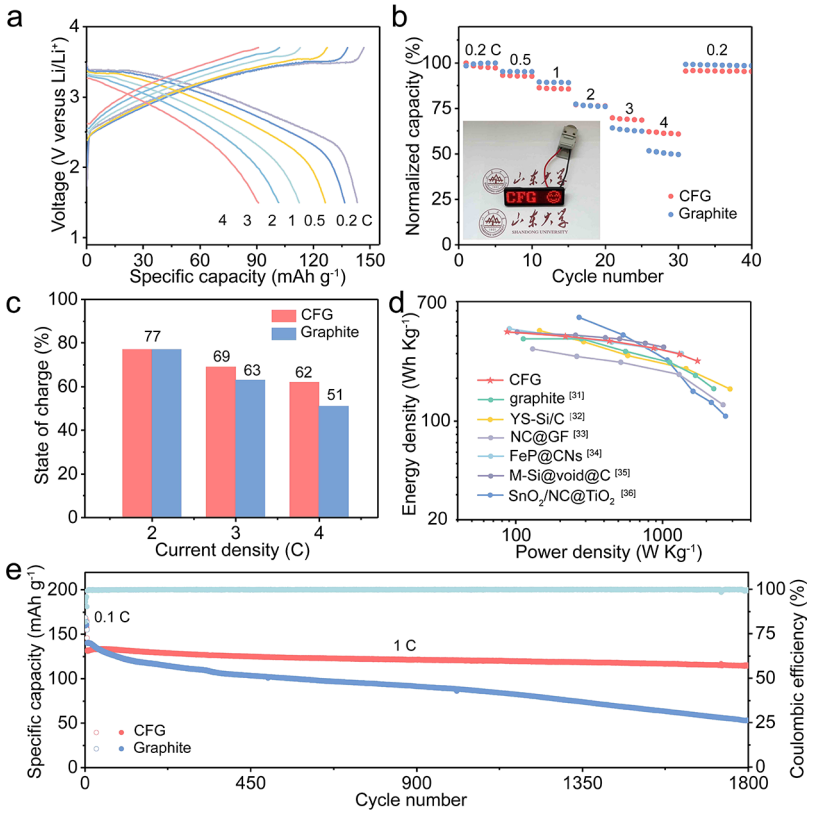

Figure 5. Electrochemical performance of the CFG//LFP full cells (1C = 150 mAh g^{-1}, based on active material in cathode). (a) Charge/discharge profiles of LFP//CFG full cells at different currents; (b) rate performance between 0.2 and 4 C; (c) plot of SOC of CFG and graphite at each current density; (d) Ragone plot; (e) cycling performance of the CFG//LFP full cells at 1C.

demonstrate that ion transport in the CFG electrode mainly originates from the fast surface-controlled capacitive behavior. This might be due to the presence of both surface Li adsorption and Li diffusion between short ordered-range graphene planes.[28] To quantify the contribution of capacitive and diffusion effects to the total capacity, their ratios are calculated based on the following formula: $i(V) = k_1v + k_2v^{1/2}$, where k_1v and $k_2v^{1/2}$ represent capacitive contribution and intercalation storage contribution, respectively.[27,28] The ratio of the capacitive contribution increases from 59 to 83% with the increase of the scan rate from 0.1 to 1.0 mV s^{-1} (Figure 4c), implying that the charge storage of the CFG is dominated by the capacitive controlled process, especially at high scan rates. The capacitive-controlled contributions are larger than 80% at 0.8 and 1.0 mV s^{-1}, as illustrated in Figure 4d. Moreover, the capacitive contribution of the CFG anode is higher than that of the FG electrode at each scan rate, which explains the better rate performance of the CFG electrode. The high capacitive contribution could be ascribed to the large specific surface area, the enlarged interlayer spacing, and short ion diffusion lengths of the CFG electrode.

Furthermore, the galvanostatic intermittent titration technique (GITT) was applied to study the Li^+ diffusion coefficient (D_{Li+}). It is mentioned that due to the low capacities of FG and CB electrodes, the corresponding GITT tests have been omitted. Figure 4e shows the GITT profiles of the CFG and graphite electrodes and the corresponding D_{Li+} values (calculation details are described in the SI). The D_{Li+} value of the CFG electrodes remains stable during both lithiation and delithiation processes (3.07×10^{-11} to 4.57×10^{-10} cm^2 s^{-1}). In contrast, the D_{Li+} values vary by several orders of magnitude in the lithiation/delithiation processes (1.81×10^{-13} to 2.69×10^{-10} cm^2 s^{-1}). Although the D_{Li+} values of the graphite are slightly higher in the initial delithiation states of 30%, the numbers are much smaller than that of the CFG in further processes, eventually resulting in poorer rate performance. The extra oxygen dopants and defect sites of the short-range ordered structure in the CFG might be responsible for the fast Li^+ diffusion.

It is widely accepted that the Li^+ conductivity is associated with electrical conductivity.[29] However, the electrical conductivity of the four samples are similar to each other (25.5, 27, 36.9, and 37.4 S m^{-1} for graphite, FG, CFG, and CB, respectively; Figure S19), which indicates that the conductivity would not be a liming factor to these electrode materials. Furthermore, the electrochemical impedance spectroscopy (EIS) was performed to investigate the charge transfer behavior in the electrodes. Figure 4f shows the corresponding Nyquist plots, where the CFG electrode exhibits the smallest semicircle diameter at the high−medium-frequency region among these four electrodes, indicating the fastest Li^+ diffusion with the lowest charge transfer resistance.[10] Moreover, the diffusion coefficient could be obtained by fitting the slope of the Z' versus $\omega^{-1/2}$ plot,[30] as demonstrated in Figure S20. The CFG exhibits the highest D_{Li+} value (5.44×10^{-12} cm^2 s^{-1}; Table S2) among these electrodes, which is about 5 times higher than the other three electrodes. In addition, EIS characterizations of the CFG electrode at different cycles (Figure S21) were carried out to track the charge transfer kinetics. The large impedance in the initial cycle could be attributed to the poor wettability of the electrolyte on the electrode material. The impedance of the CFG electrode

https://doi.org/10.1021/acsanm.2c04717
ACS Appl. Nano Mater. XXXX, XXX, XXX−XXX

gradually decreases from pristine to the 50th cycle, indicating faster charge transfer kinetics after cycling.

To further evaluate the capability of the CFG to achieve fast-charging LIBs, a full cell was assembled using the CFG and $LiFePO_4$ (LFP) as the anode and cathode, respectively. Prior to the full cell assembly, the commercial LFP cathode was tested (Figure S22), which exhibits excellent rate performance and reversibility. Figure S23 shows the reversible voltage profile versus Li of the CFG and the LFP at 0.1 C. The LFP cathode exhibits a steady working potential of 3.4 V with a reversible capacity of 152 mAh g^{-1}, while the CFG anode shows continuous and plateau-free charge−discharge curves with a reversible capacity of 550 mAh g^{-1}. The CFG//LFP full cell delivers a discharge capacity of 144 mAh g^{-1} at 0.2 C with an average voltage of 2.9 V (Figure 5a). The state of charge (SOC) is 93, 86, 77, 69, and 62% at 0.5, 1, 2, 3, and 4 C, respectively (Figure 5b). Strikingly, the SOC of the CFG//LFP full cell reaches 77% at 2 C, indicating that the full cell using the CFG anode has reached the level of fast charging.[4] To highlight the practical application of the full cell, a light-emitting-diode array is lightened as shown in the inset of Figure 5b. Remarkably, at a higher charging rate, the CFG-based full cell exhibits higher SOC than that of the graphite-based one (Figure 5c). Moreover, the energy densities and power densities of various representative anode and LFP cathode full cells are summarized in the form of Ragone plots as in Figure 5d.[31−36] The CFG//LFP full cell could deliver a high energy of 265 Wh kg^{-1} at a high power density of 1740 W kg^{-1}, which shows a slower decay compared to that of the graphite//LFP full cell, and is superior to many other anode-based full cells. Additionally, the CFG//LFP full cell maintains stable cycling behavior over 1800 cycles, with a high capacity retention of 88% at 1 C and nearly 100% CE (Figure 5e). To the best of our knowledge, the outstanding cycling life of the full cell is superior to almost all carbon-based full cells (Table S3), demonstrating its great practical applicability.

CONCLUSIONS

In summary, we have introduced the FJH implementation to realize gram-scale production of FG and subsequent BM treatment to obtain CFG. The CFG has shortened in-plane ordered ranges and larger interlayer spacings than its parental FG, leading to open channels and shortened pathways for Li^+ transport. As a result, the CFG anode exhibits high specific capacity and excellent rate performance, which outperforms FG, commercial carbon black, and graphite electrodes. Moreover, it shows ultrastable cycling performance with a high capacity retention of 99% at the 500th cycle. Moreover, the CFG anode shows good compatibility with the $LiFePO_4$ cathode, which enables a fast-charging LIB full battery with a SOC of 77 and 62% at 2C and 4C, respectively. This work provides a low-cost and high-throughput way to produce fast-charging LIB anodes, which is practical to use for commercial fast-charging LIBs.

EXPERIMENTAL SECTION

Synthesis of FG. FG was prepared according to the previously reported method.[14] Commercial carbon black (CB) was packed between two copper electrodes in a quartz tube. In a vacuum desiccator, a homemade setup is connected to the copper electrode with a voltage of 110 V and current of 0.1 A applied to the sample for 100−200 ms to purify the carbon precursor. About 200 mg of FG can be obtained in one batch (230 mg of CB) using a quartz tube with a diameter of 1.5 cm. The percent yield of FG is about 85 to 90%.

Synthesis of CFG. The CFG was obtained by the BM method in the planetary mill at a frequency of 50 Hz for 60 min. The BM was carried out with a ball-to-sample weight ratio of 100:1 (20 g of stainless-steel balls and 0.2 g of FG) in a 25 mL ball mill jar. The ball mill jar was sealed in an Ar-filled glove box before the BM operation.

Electrochemical Measurements. Galvanostatic charge/discharge tests and cycling stability of the coin cells (CR2032) were conducted on the LAND CT2001A electrochemical workstation at room temperature.

For half cells, the slurry of the as-obtained samples, conductive acetylene black and poly(vinylidene difluoride) (PVDF) with a mass ratio of 7:2:1 in *N*-methyl pyrrolidone (NMP) was coated on Cu foil and dried in a vacuum oven at 120 °C for 12 h to prepare the working electrode. Then, the half cells were fabricated with a separator, an electrolyte, and lithium wafers as the counter electrode. The mass loading of the active materials is about 1 mg cm^{-2}. The cycling tests of the CFG electrode in half lithium were performed at various current densities (i.e., 0.05, 0.1, 0.2, 0.5, 1, 2, 3, and 5 A g^{-1}) in the 0.01−3 V voltage range. CV and EIS were measured using the electrochemical workstation (CHI 660E) at various scanning rates from 0.01 to 3 V and with a frequency range of 100 kHz to 0.01 Hz.

For full cells, the negative/positive electrode capacity (N/P) ratio is 1.2−1.6. The cathodes were prepared with 70% of commercial LFP powers, 20% conductive acetylene black, and 10% PVDF in NMP. The as-obtained slurry was spread on Al foil and dried overnight in a vacuum oven at 120 °C. The cycling of Li-LFP half cells was tested in the voltage range of 2.5−4.2 V under different current densities. Before assembling the full cells, the CFG and graphite anodes were pre-cycled to form SEI and then matched with the LFP cathodes. The graphite//LFP full cells were cycled within a voltage range from 2.5 to 3.7 V. The CFG//LFP full cells were cycled between 1.5 and 3.7 V at different current densities (i.e., 0.2 C, 0.5 C, 1 C, 2 C, 3 C, and 4 C) (1 C corresponding to 150 mA g^{-1}) based on the weight of cathode materials. The SOC was calculated based on the capacity obtained at 0.2 C.[4] The energy density and power density of the full cells were calculated based on the equations $E = \int V\,dQ$ and $P = E/t$, where E, V, Q, P, and t represent the energy density, working voltage, discharge capacity, power energy, and discharge time, respectively.[37]

$LiPF_6$ (1 M) in ethylene carbonate (EC) and dimethyl carbonate (DMC) (1:1 by volume) was used as the electrolyte for all cells. The polypropylene film (Celgard 2400) is used as the separator, and each cell requires around 70 μL of electrolyte. All the cells were assembled in an argon-filled glovebox (O_2 and H_2O < 0.1 ppm).

ASSOCIATED CONTENT

Supporting Information

The Supporting Information is available free of charge at https://pubs.acs.org/doi/10.1021/acsanm.2c04717.

Detailed information about the XRD, SEM, TEM, FTIR, XPS, and CV curves; GCD profiles; EIS; GITT; electrochemical measurements; comparison of the rate and cycle performance (PDF)

AUTHOR INFORMATION

Corresponding Authors

Hao Wu − *Institute of Molecular Sciences and Engineering, Institute of Frontier and Interdisciplinary Science, Shandong University, Qingdao, Shandong 266237, China;* orcid.org/0000-0002-9464-2033; Email: haowu2020@sdu.edu.cn

Weiqiao Deng − *Institute of Molecular Sciences and Engineering, Institute of Frontier and Interdisciplinary Science, Shandong University, Qingdao, Shandong 266237, China;* orcid.org/0000-0002-3671-5951; Email: dengwq@sdu.edu.cn

https://doi.org/10.1021/acsanm.2c04717
ACS Appl. Nano Mater. XXXX, XXX, XXX−XXX

Authors

Hongyan Yang − *Institute of Molecular Sciences and Engineering, Institute of Frontier and Interdisciplinary Science, Shandong University, Qingdao, Shandong 266237, China*

Lanju Sun − *Institute of Molecular Sciences and Engineering, Institute of Frontier and Interdisciplinary Science, Shandong University, Qingdao, Shandong 266237, China*

Shengliang Zhai − *Institute of Molecular Sciences and Engineering, Institute of Frontier and Interdisciplinary Science, Shandong University, Qingdao, Shandong 266237, China*

Xiao Wang − *Institute of Molecular Sciences and Engineering, Institute of Frontier and Interdisciplinary Science, Shandong University, Qingdao, Shandong 266237, China*

Chengcheng Liu − *Institute of Molecular Sciences and Engineering, Institute of Frontier and Interdisciplinary Science, Shandong University, Qingdao, Shandong 266237, China*

Complete contact information is available at: https://pubs.acs.org/10.1021/acsanm.2c04717

Notes

The authors declare no competing financial interest.

■ ACKNOWLEDGMENTS

We thank the financial support from the Science Foundation for Outstanding Young Scholars of Shandong Province (no. 2022HWYQ-009), the Natural Science Foundation of Shandong Province (nos. ZR2021QB201 and YDZX2021001), and the Qilu Young Scholars Program of Shandong University.

■ REFERENCES

(1) Lee, J.; Kim, C.; Cheong, J. Y.; Kim, I. D. An Angstrom-level d-spacing Control of Graphite Oxide Using Organofillers for High-Rate Lithium Storage. *Chem* **2022**, *8*, 2393−2409.

(2) Lee, M. J.; Lee, K.; Lim, J.; Li, M.; Noda, S.; Kwon, S. J.; DeMattia, B.; Lee, B.; Lee, S. W. Outstanding Low-Temperature Performance of Structure-Controlled Graphene Anode Based on Surface-Controlled Charge Storage Mechanism. *Adv. Funct. Mater.* **2021**, *31*, 2009397.

(3) Li, X.; Zhi, L. Graphene Hybridization for Energy Storage Applications. *Chem. Soc. Rev.* **2018**, *47*, 3189−3216.

(4) Zhu, G. L.; Zhao, C. Z.; Huang, J. Q.; He, C.; Zhang, J.; Chen, S.; Xu, L.; Yuan, H.; Zhang, Q. Fast Charging Lithium Batteries: Recent Progress and Future Prospects. *Small* **2019**, *15*, 1805389.

(5) Kim, N.; Chae, S.; Ma, J.; Ko, M.; Cho, J. Fast-charging High-Energy Lithium-Ion Batteries via Implantation of Amorphous Silicon Nanolayer in Edge-Plane Activated Graphite Anodes. *Nat. Commun.* **2017**, *8*, 812.

(6) Cai, W.; Yao, Y. X.; Zhu, G. L.; Yan, C.; Jiang, L. L.; He, C.; Huang, J. Q.; Zhang, Q. A Review on Energy Chemistry of Fast-Charging Anodes. *Chem. Soc. Rev.* **2020**, *49*, 3806−3833.

(7) Lu, L. L.; Lu, Y. Y.; Zhu, Z. X.; Shao, J. X.; Yao, H. B.; Wang, S.; Zhang, T. W.; Ni, Y.; Wang, X. X.; Yu, S. H. Extremely Fast-Charging Lithium Ion Battery Enabled by Dual-Gradient Structure Design. *Sci. Adv.* **2022**, *8*, eabm6624.

(8) Xie, L.; Tang, C.; Bi, Z.; Song, M.; Fan, Y.; Yan, C.; Li, X.; Su, F.; Zhang, Q.; Chen, C. Hard Carbon Anodes for Next-Generation Li-Ion Batteries: Review and Perspective. *Adv. Energy Mater.* **2021**, *11*, 2101650.

(9) Andersen, H. L.; Djuandhi, L.; Mittal, U.; Sharma, N. Strategies for the Analysis of Graphite Electrode Function. *Adv. Energy Mater.* **2021**, *11*, 2102693.

(10) Mo, R.; Li, F.; Tan, X.; Xu, P.; Tao, R.; Shen, G.; Lu, X.; Liu, F.; Shen, L.; Xu, B.; Xiao, Q.; Wang, X.; Wang, C.; Li, J.; Wang, G.; Lu, Y. High-Quality Mesoporous Graphene Particles as High-Energy and Fast-Charging Anodes for Lithium-Ion Batteries. *Nat. Commun.* **2019**, *10*, 1474.

(11) Wu, C. H.; Pu, N. W.; Liu, Y. M.; Chen, C. Y.; Peng, Y. Y.; Cheng, T. Y.; Lin, M. H.; Ger, M. D. Improving Rate Capability of Lithium-Ion Batteries Using Holey Graphene as the Anode Material. *J. Taiwan Inst. Chem. Eng.* **2017**, *80*, 511−517.

(12) Lin, L.; Peng, H.; Liu, Z. Synthesis Challenges for Graphene Industry. *Nat. Mater.* **2019**, *18*, 520−524.

(13) Wyss, K. M.; Luong, D. X.; Tour, J. M. Large-Scale Syntheses of 2D Materials: Flash Joule Heating and Other Methods. *Adv. Mater.* **2022**, *34*, 2106970.

(14) Luong, D. X.; Bets, K. V.; Algozeeb, W. A.; Stanford, M. G.; Kittrell, C.; Chen, W.; Salvatierra, R. V.; Ren, M.; McHugh, E. A.; Advincula, P. A.; Wang, Z.; Bhatt, M.; Guo, H.; Mancevski, V.; Shahsavari, R.; Yakobson, B. I.; Tour, J. M. Gram-Scale Bottom-Up Flash Graphene Synthesis. *Nature* **2020**, *577*, 647−651.

(15) Li, G. Regulating Mass Transport Behavior for High-Performance Lithium Metal Batteries and Fast-Charging Lithium-Ion Batteries. *Adv. Energy Mater.* **2021**, *11*, 2002891.

(16) Jiang, Y.; Song, D.; Wu, J.; Wang, Z.; Huang, S.; Xu, Y.; Chen, Z.; Zhao, B.; Zhang, J. Sandwich-like SnS_2/Graphene/SnS_2 with Expanded Interlayer Distance as High-Rate Lithium/Sodium-Ion Battery Anode Materials. *ACS Nano* **2019**, *13*, 9100−9111.

(17) Dong, Y.; Lin, X.; Wang, D.; Yuan, R.; Zhang, S.; Chen, X.; Bulusheva, L. G.; Okotrub, A. V.; Song, H. Modulating the Defects of Graphene Blocks by Ball-Milling for Ultrahigh Gravimetric and Volumetric Performance and Fast Sodium Storage. *Energy Stor. Mater.* **2020**, *30*, 287−295.

(18) Jeon, I. Y.; Shin, Y. R.; Sohn, G. J.; Choi, H. J.; Bae, S. Y.; Mahmood, J.; Jung, S. M.; Seo, J. M.; Kim, M. J.; Wook Chang, D.; Dai, L.; Baek, J. B. Edge-Carboxylated Graphene Nanosheets via Ball Milling. *Proc. Natl. Acad. Sci. U. S. A.* **2012**, *109*, 5588−5593.

(19) Dong, Y.; Zhang, S.; Du, X.; Hong, S.; Zhao, S.; Chen, Y.; Chen, X.; Song, H. Boosting the Electrical Double-Layer Capacitance of Graphene by Self-Doped Defects through Ball-Milling. *Adv. Funct. Mater.* **2019**, *29*, 1901127.

(20) Zhang, Y.; Ma, Q.; Wang, S.; Liu, X.; Li, L. Poly(vinyl alcohol)-Assisted Fabrication of Hollow Carbon Spheres/Reduced Graphene Oxide Nanocomposites for High-Performance Lithium-Ion Battery Anodes. *ACS Nano* **2018**, *12*, 4824−4834.

(21) Wang, Z.; Xu, W.; Chen, X.; Peng, Y.; Song, Y.; Lv, C.; Liu, H.; Sun, J.; Yuan, D.; Li, X.; Guo, X.; Yang, D.; Zhang, L. Defect-Rich Nitrogen Doped Co_3O_4/C Porous Nanocubes Enable High-Efficiency Bifunctional Oxygen Electrocatalysis. *Adv. Funct. Mater.* **2019**, *29*, 1902875.

(22) Chen, J.; Mao, Z.; Zhang, L.; Wang, D.; Xu, R.; Bie, L.; Fahlman, B. D. Nitrogen-Deficient Graphitic Carbon Nitride with Enhanced Performance for Lithium Ion Battery Anodes. *ACS Nano* **2017**, *11*, 12650−12657.

(23) Ma, C.; Zhao, Y.; Li, Y. A Facile Solution-Free Etching Preparation of Porous Graphene Nanosheets with High Performances for Lithium Storage. *Chem. Eng. J.* **2017**, *320*, 283−289.

(24) Zhong, M.; Yan, J.; Wu, H.; Shen, W.; Zhang, J.; Yu, C.; Li, L.; Hao, Q.; Gao, F.; Tian, Y.; Huang, Y.; Guo, S. Multilayer Graphene Spheres Generated from Anthracite and Semi-Coke as Anode Materials for Lithium-Ion Batteries. *Fuel Process. Technol.* **2020**, *198*, No. 106241.

(25) Xing, B.; Zeng, H.; Huang, G.; Zhang, C.; Yuan, R.; Cao, Y.; Chen, Z.; Yu, J. Porous Graphene Prepared from Anthracite as High Performance Anode Materials for Lithium-Ion Battery Applications. *J. Alloys Compd.* **2019**, *779*, 202−211.

(26) Jiang, Z.; Pei, B.; Manthiram, A. Randomly Stacked Holey Graphene Anodes for Lithium Ion Batteries with Enhanced Electrochemical Performance. *J. Mater. Chem. A* **2013**, *1*, 7775−7781.

(27) Yi, Y.; Li, J.; Zhao, W.; Zeng, Z.; Lu, C.; Ren, H.; Sun, J.; Zhang, J.; Liu, Z. Temperature-Mediated Engineering of Graphdiyne

Framework Enabling High-Performance Potassium Storage. *Adv. Funct. Mater.* **2020**, *30*, 2003039.
(28) Scaravonati, S.; Sidoli, M.; Magnani, G.; Morenghi, A.; Canova, M.; Kim, J. H.; Ricco, M.; Pontiroli, D. Combined Capacitive and Electrochemical Charge Storage Mechanism in High-performance Graphene-based Lithium-ion Batteries. *Mater. Today Energy* **2022**, *24*, No. 100928.
(29) Tian, T.; Lu, L. L.; Yin, Y. C.; Li, F.; Zhang, T. W.; Song, Y. H.; Tan, Y. H.; Yao, H. B. Multiscale Designed Niobium Titanium Oxide Anode for Fast Charging Lithium Ion Batteries. *Adv. Funct. Mater.* **2021**, *31*, 2007419.
(30) Bi, W.; Gao, G.; Wu, G.; Atif, M.; AlSalhi, M. S.; Cao, G. Sodium Vanadate/PEDOT Nanocables Rich with Oxygen Vacancies for High Energy Conversion Efficiency Zinc Ion Batteries. *Energy Stor. Mater.* **2021**, *40*, 209−218.
(31) Mu, Y.; Han, M.; Li, J.; Liang, J.; Yu, J. Growing Vertical Graphene Sheets on Natural Graphite for Fast Charging Lithium-Ion Batteries. *Carbon* **2021**, *173*, 477−484.
(32) Zhang, L.; Wang, C.; Dou, Y.; Cheng, N.; Cui, D.; Du, Y.; Liu, P.; Al-Mamun, M.; Zhang, S.; Zhao, H. A Yolk-Shell Structured Silicon Anode with Superior Conductivity and High Tap Density for Full Lithium-Ion Batteries. *Angew. Chem., Int. Ed.* **2019**, *58*, 8824−8828.
(33) Huang, Y.; Li, K.; Yang, G.; Aboud, M. F. A.; Shakir, I.; Xu, Y. Ultrathin Nitrogen-Doped Carbon Layer Uniformly Supported on Graphene Frameworks as Ultrahigh-Capacity Anode for Lithium-Ion Full Battery. *Small* **2018**, *14*, 1703969.
(34) Zheng, Z.; Wu, H. H.; Liu, H.; Zhang, Q.; He, X.; Yu, S.; Petrova, V.; Feng, J.; Kostecki, R.; Liu, P.; Peng, D. L.; Liu, M.; Wang, M. S. Achieving Fast and Durable Lithium Storage through Amorphous FeP Nanoparticles Encapsulated in Ultrathin 3D P-Doped Porous Carbon Nanosheets. *ACS Nano* **2020**, *14*, 9545−9561.
(35) Wang, F.; Wang, B.; Ruan, T.; Gao, T.; Song, R.; Jin, F.; Zhou, Y.; Wang, D.; Liu, H.; Dou, S. Construction of Structure-Tunable Si@Void@C Anode Materials for Lithium-Ion Batteries through Controlling the Growth Kinetics of Resin. *ACS Nano* **2019**, *13*, 12219−12229.
(36) Wei, D.; Zhong, S.; Zhang, H.; Zhang, X.; Zhu, C.; Duan, J.; Li, L.; Chen, Z.; Liu, P.; Zhang, G.; Duan, H. In Situ Construction of Interconnected SnO_2/Nitrogen-Doped Carbon@TiO_2 Networks for Lithium-Ion Half/Full Cells. *Electrochim. Acta* **2018**, *290*, 312−321.
(37) Xu, X.; Zhang, Y.; Sun, H.; Zhou, J.; Liu, Z.; Qiu, Z.; Wang, D.; Yang, C.; Zeng, Q.; Peng, Z.; Guo, S. Orthorhombic Cobalt Ditelluride with Te Vacancy Defects Anchoring on Elastic MXene Enables Efficient Potassium Ion Storage. *Adv. Mater.* **2021**, *33*, 2100272.

https://doi.org/10.1021/acsanm.2c04717
ACS Appl. Nano Mater. XXXX, XXX, XXX−XXX